nature physics

LETTERS

https://doi.org/10.1038/s41567-018-0078-z

Anomalous Hall effect in $ZrTe_5$

Tian Liang[1,2,3,7*], Jingjing Lin[1,7], Quinn Gibson[4], Satya Kushwaha[4], Minhao Liu[1], Wudi Wang[1], Hongyu Xiong[2,3], Jonathan A. Sobota[2,3,5], Makoto Hashimoto[6], Patrick S. Kirchmann[3], Zhi-Xun Shen[2,3], R. J. Cava[4] and N. P. Ong[1*]

Research in topological matter has expanded to include the Dirac and Weyl semimetals[1–10], which feature three-dimensional Dirac states protected by symmetry. Zirconium pentatelluride has been of recent interest as a potential Dirac or Weyl semimetal material. Here, we report the results of experiments performed by in situ three-dimensional double-axis rotation to extract the full 4π solid angular dependence of the transport properties. A clear anomalous Hall effect is detected in every sample studied, with no magnetic ordering observed in the system to the experimental sensitivity of torque magnetometry. Large anomalous Hall signals develop when the magnetic field is rotated in the plane of the stacked quasi-two-dimensional layers, with the values vanishing above about 60 K, where the negative longitudinal magnetoresistance also disappears. This suggests a close relation in their origins, which we attribute to the Berry curvature generated by the Weyl nodes.

Zirconium pentatelluride ($ZrTe_5$) has recently attracted considerable attention, following the observation of negative longitudinal magnetoresistance (LMR)[11]. This negative LMR has been identified with the chiral anomaly[12–14] that is predicted to occur in Dirac and Weyl semimetals[1–10] and was recently observed in Na_3Bi and GdPtBi[15,16]. However, despite the observation of the negative LMR, there are no theoretical predictions showing that $ZrTe_5$ is a three-dimensional (3D) Dirac or Weyl semimetal, in contrast to both Na_3Bi (ref. [17]) and Cd_3As_2 (ref. [18]). Furthermore, the results of angle-resolved photoemission spectroscopy (ARPES) experiments[11,19–23] are not yet conclusive.

It is therefore of interest to investigate other unusual transport properties of $ZrTe_5$, especially the Hall response engendered by the Berry curvature. For Dirac and Weyl semimetals in an electric field $\mathbf{E}$, a finite Berry curvature leads to an anomalous velocity $\mathbf{v}_A = \mathbf{E} \times \mathbf{\Omega}_\mathbf{k}$, which produces the anomalous Hall conductivity

$$\sigma_{xy}^{\mathrm{AHE}} = \sum_{i,\mathbf{k}} n_{i,\mathbf{k}}\ \mathbf{\Omega}_{i,\mathbf{k}}^{z} \qquad (1)$$

where the index i runs over the Weyl nodes, and n_i is the occupation number in node i. Depending on the chirality χ_i, $\mathbf{\Omega}_{i,\mathbf{k}}$ is directed either radially inwards or outwards. Close to the node at $\mathbf{K}_i$, the Berry curvature has a monopole form $\mathbf{\Omega}_{i,\mathbf{k}} = \chi_i\ \Delta\mathbf{k}_i/|\Delta\mathbf{k}_i|^3$, where $\Delta\mathbf{k}_i = \mathbf{k} - \mathbf{K}_i$ (ref. [24]). The anomalous Hall effect (AHE) arises even for non-magnetic systems. This is because, in $\mathbf{k}$-space, the Weyl nodes behave as effective magnetic monopoles, generating strong Berry curvature $\mathbf{\Omega}_\mathbf{k}$ that acts like an effective magnetic field. To characterize $ZrTe_5$ in more detail, we have obtained the full 4π solid angular dependence of the anomalous Hall signals, that is $\mathbf{\Omega}_\mathbf{k}$, using in situ 3D double-axis rotation Hall measurements.

$ZrTe_5$ has an orthorhombic layered structure with space group $Cmcm$ (D_{2h}^{17})[25] (inset in Fig. 1a). The $ZrTe_6$ triangular prisms (depicted as the red dashed lines) form one-dimensional chains of $ZrTe_3$ running along the a axis. The chains are connected by additional Te ions, which also form zigzag chains along the a axis and extend along the c axis. As a result, they define quasi-two-dimensional layers that stack along the b axis via van der Waals interactions to form the 3D crystal. The magnitude of the van der Waals interaction along the b axis is very small, comparable to that in graphite[25]. Therefore, both the two-dimensional single layer and the 3D bulk crystals of $ZrTe_5$ are of interest. A monolayer of $ZrTe_5$ is predicted to feature the quantum spin Hall state, while 3D bulk $ZrTe_5$ is predicted to lie near the boundary separating a weak toplogical insulator and a strong topological insulator[25]. We studied 3D bulk crystals in our experiments.

The transport properties of $ZrTe_5$ were investigated with the current applied along the chain axis a. Figure 1a shows that the resistivity ρ in our samples increases with decreasing temperature T down to the lowest T, where ρ saturates. Published resistivity curves[26,27] show resistivity profiles with maxima occurring at a temperature T_0, which varies from 135 K (ref. [28]) to 65 K (ref. [11]). T_0 can be systematically decreased by chemical pressure induced by substitution of rare earth elements[27]. For our samples, $T_0 \lesssim 5$ K. In ARPES experiments on samples with $T_0 = 135$ K, multiple bands were observed at low T (for example 35 K)[20]. At a casual glance, this raises concerns that multiple bands may contribute to the AHE here. However, this is not the case for our samples, for which $T_0 \lesssim 5$ K. The key difference is that while the samples with $T_0 = 135$ K show two electron pockets at low T (35 K), in our $ZrTe_5$ samples the ARPES measurements detect only a single hole pocket situated at Γ (Fig. 1c).

Since our interest is in the AHE arising from $\mathbf{\Omega}_\mathbf{k}$ produced by Weyl nodes, it is important to check that the AHE signal is not associated with conventional ferromagnetism. For this purpose, we have performed torque magnetometry measurements. The results are shown in Fig. 1b for selected samples. No magnetic ordering is observed, confirming that the AHE in $ZrTe_5$, shown in Figs. 2–4, does not come from magnetism. This is as expected, since $ZrTe_5$ does not contain magnetic elements.

The first clue for a large Berry curvature in $ZrTe_5$ came from Hall measurements in sample Z2 with the magnetic field $\mathbf{H}$ lying in the

[1]Department of Physics, Princeton University, Princeton, NJ, USA. [2]Geballe Laboratory for Advanced Materials, Departments of Physics and Applied Physics, Stanford University, Stanford, CA, USA. [3]Stanford Institute for Materials and Energy Sciences, SLAC National Accelerator Laboratory, Menlo Park, CA, USA. [4]Department of Chemistry, Princeton University, Princeton, NJ, USA. [5]Advanced Light Source, Lawrence Berkeley National Laboratory, Berkeley, CA, USA. [6]Stanford Synchrotron Radiation Lightsource, SLAC National Accelerator Laboratory, Menlo Park, CA, USA. [7]These authors contributed equally: Tian Liang, Jingjing Lin. *e-mail: liang16@stanford.edu; npo@princeton.edu

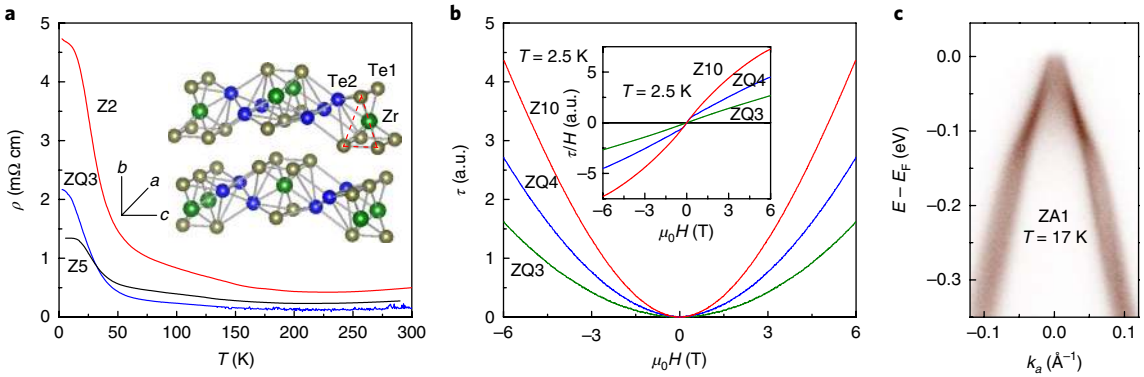

Fig. 1 | Resistivity, magnetization and ARPES spectrum of $ZrTe_5$. **a**, ρ versus T for $ZrTe_5$ (samples Z2, Z5 and ZQ3). As T decreases from 200 K, $\rho(T)$ increases monotonically but approaches saturation below 20 K. The inset shows the crystal structure of $ZrTe_5$. **b**, Torque signal τ versus H measured at 2.5 K (samples Z10, ZQ3 and ZQ4). The inset shows magnetization τ/H. The quadratic behaviour of τ versus H implies that the dominant contribution is either a paramagnetic or diamagnetic response. The absence of any anomaly in τ/H at weak H rules out magnetic ordering in samples Z10 and ZQ3. In sample ZQ4 a weak anomaly is resolved, but it occurs below 0.3 T, whereas the AHE signal onsets above ~1 T. From the accumulated data in all samples, we conclude that the AHE signal and torque anomaly in ZQ4 are unrelated (all samples investigated show the AHE signal but ZQ4 is the only one to display a torque anomaly). **c**, ARPES data along a momentum cut parallel to the chain axis a, measured from the Fermi energy E_F, for sample ZA1 measured at $T = 17$ K with incident photon energy of 6 eV. The ARPES spectrum reveals a single hole band.

ab plane (Fig. 2). The resistivity ρ_{xx} versus H (Fig. 2a) displays a negative LMR in a narrow range of $\theta \lesssim 1°$, where θ is the angle between **H** and **a**. This confirms the results reported in ref. [11]. Interestingly, the Hall resistivity ρ_{yx} shows a very unusual zigzag profile, suggestive of an anomalous contribution (Fig. 2b). By subtraction of the high-field, linear positive background (the ordinary Hall signal of

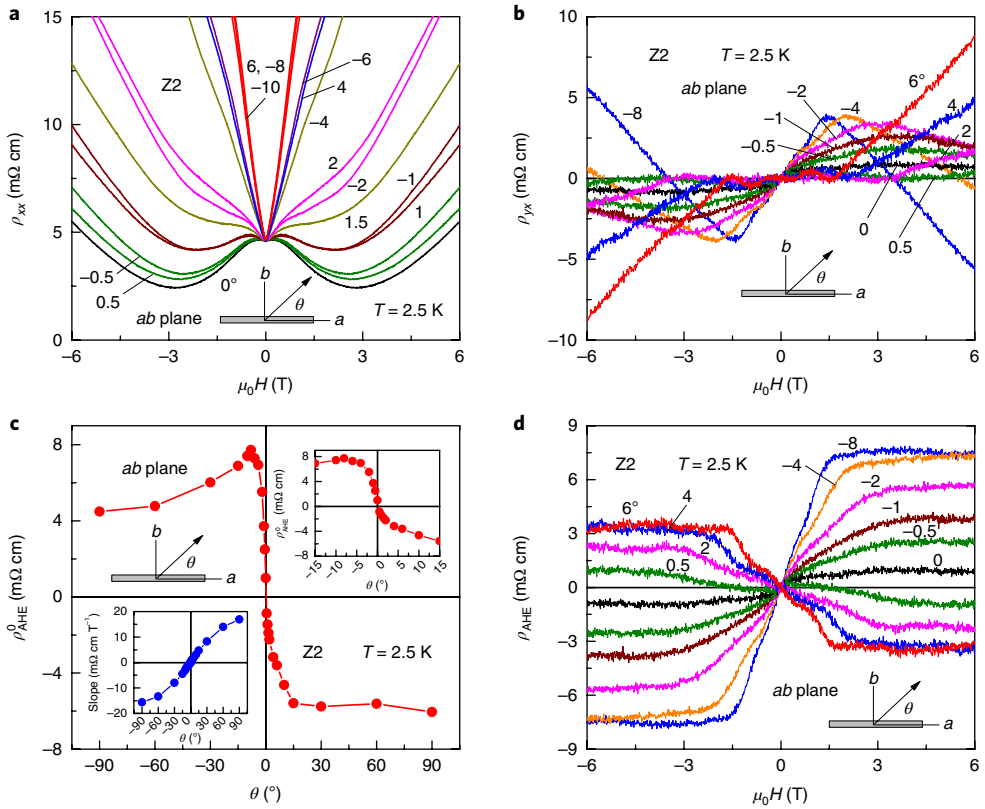

Fig. 2 | Angular dependence of MR and Hall signals in sample Z2. H lies within the *ab* plane at selected θ (inset). **a**, Variations of ρ_{xx} versus H at selected θ. Negative LMR is observed in a small angular regime $\theta \lesssim 1°$. **b**, Hall data at selected θ reveal a highly unusual zigzag pattern that suggests a dominant anomalous Hall contribution. **c**, Full angular dependence of the anomalous Hall contribution ρ^0_{AHE} obtained from **d**. The upper right inset shows ρ^0_{AHE} at small angles and the lower left inset shows the angular dependence of the background slope. **d**, ρ_{AHE} after removal of the high-field linear background (the ordinary Hall term) from the curves in **b**. At fixed θ, the AHE curves are antisymmetric with respect to H. However, plotted as a function of θ (**c**), ρ_{AHE} is distorted by a large, in-plane Hall contribution acquired by a slight misalignment. This observation motivated the double-axis Hall measurements.

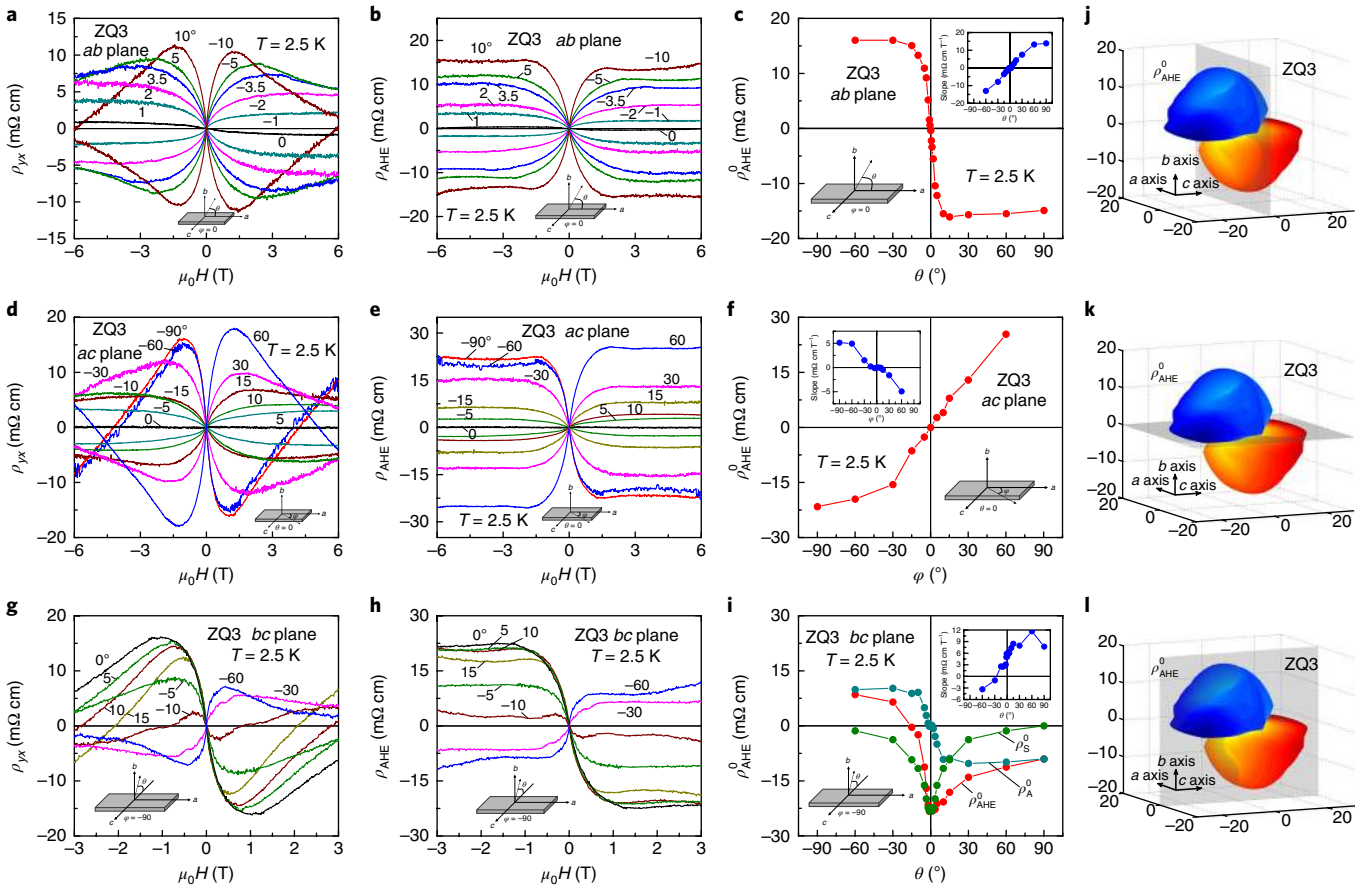

Fig. 3 | Full 4π solid angular dependence of AHE in sample ZQ3. In each panel, θ and φ are defined in the insets. **a**,**b**,**c**, When **H** is rotated in the *ab* plane (out of plane), a large AHE signal is observed with the anomalous component from **Ωk** saturating rapidly as **H** is tilted away from the *a* axis. **d**,**e**,**f**, Significantly, even when **H** is rotated in the *ac* plane (in plane), a large AHE Hall signal is observed. The in-plane AHE signal is rigorously antisymmetric in both *H* and φ (hence a 'true' Hall signal). **g**,**h**,**i**, Finally, when **H** is rotated in the *bc* plane, the observed Hall signal is a mixture of the AHE, consistent with the angular variation of **Ωk** shown in **i**. The antisymmetrized resistivity (see text) $\rho_A(\theta) = (\rho_{AHE}(\theta) - \rho_{AHE}(-\theta))/2$ (dark cyan line in **i**) matches the Berry curvature obtained from measurements in the *ab* plane. In contrast, the symmetrized combination $\rho_S(\theta) = (\rho_{AHE}(\theta) + \rho_{AHE}(-\theta))/2$ (olive line in **i**) does not match the *ac*-plane profile in **f**. We hypothesize that there are two distinct types of Weyl pair. **j**,**k**,**l**, The 3D polar plots of ρ^0_{AHE}, represented by the vector (r, θ, φ) (orange and blue represent positive and negative values, respectively). The principal planes are depicted in grey.

the hole carriers), we isolate the anomalous component, which is shown in Fig. 2d. The angular dependence of the magnitude of the anomalous Hall contribution in Fig. 2c shows that the Berry curvature grows rapidly as soon as **H** is tilted away from **a** by a finite angle θ. This implies a sharp sensitivity of $\mathbf{\Omega}_\mathbf{k}$ to the direction of **H**. The AHE contribution is antisymmetric with respect to **H** at fixed θ. However, the antisymmetry with respect to θ is distorted (see Fig. 2c,d) by an additional contribution, which arises from a large in-plane Hall effect picked up by a slight misalignment.

To understand the in-plane Hall contribution, we made detailed measurements using a double-axis rotator to acquire the AHE signal in sample ZQ3 over the full 4π solid angle. This is plotted in Fig. 3 as a function of the two angles φ and θ, with the angular direction of **H** defined in the insets. Figure 3j–l shows a 3D polar representation of the AHE signal, as the vector (r, θ, φ) where r is proportional to the AHE signal, or effectively $|\mathbf{\Omega}_\mathbf{k}|$. When carefully aligned using the double-axis rotator, the out-of-plane (*ab*-plane) AHE signals are antisymmetric with respect to both *H* and θ (see Fig. 3a–c).

Next, we focus on the contribution from the in-plane component of **H** (in the *ac* plane). With **H** in plane and at an angle φ to **a**, we observe remarkably large AHE signals at each value of φ except when $\mathbf{H}||a$ ($\varphi = 0$) (see Fig. 3d–f). The AHE contribution is much less sensitive to tilt angle, compared with the *ab*-plane experiment—its amplitude saturates rather gradually with increasing φ. We remark that this 'true' planar Hall signal is anomalous. It is rigorously antisymmetric in *H* as well as in φ. Obviously, the conventional Lorentz force cannot produce a Hall signal with **H** in plane. However, the experimental results show that there is a large contribution of the AHE, comparable to or even larger than that from out-of-plane (*ab*-plane) field. The evidence strongly supports a large Berry curvature arising from Weyl nodes.

We emphasize that the planar Hall signal described here is very different from the so-called 'planar Hall effect' V_{xy} observed using transverse voltage probes in conventional, planar angular magnetoresistance (AMR) experiments on thin films of a ferromagnet or any high-mobility semimetal as **H** is rotated in the plane. In such AMR experiments, V_{xy} is strictly symmetric in *H*, and hence is not a true Hall signal obeying Onsager's theorem for the Hall conductivity $\sigma_{xy}(\mathbf{H}) = \sigma_{yx}(-\mathbf{H})$. For clarity, we refer to the transverse voltage in AMR experiments as the 'off-diagonal AMR' signal.

Recent studies[29,30] proposed the 'planar Hall effect' in Weyl systems. At first glance, their predictions seem relevant to our Hall results. However, this is not the case. The planar signal in refs [29,30] is strictly symmetric in *H*, and hence an example of an off-diagonal AMR signal, whereas the in-plane AHE signal uncovered in $ZrTe_5$ is strictly antisymmetric in both *H* and φ.

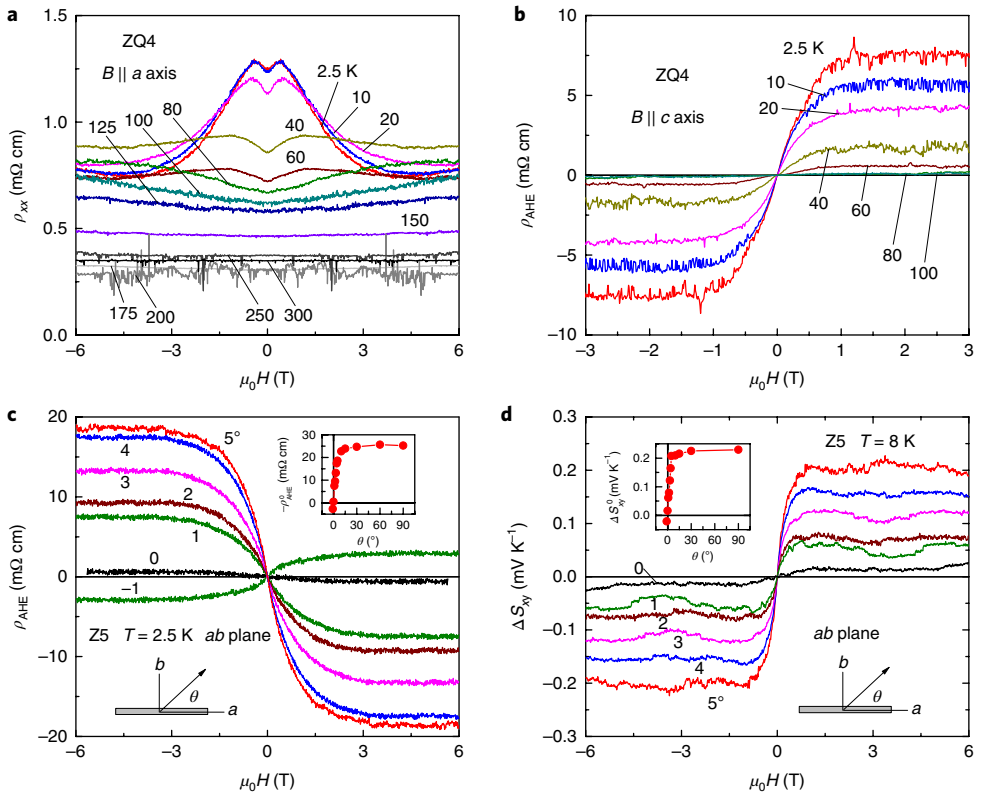

Fig. 4 | Temperature and angular dependence of transport properties in samples ZQ4 and Z5. a,**b**, The negative LMR and AHE in sample ZQ4. **c**,**d**, The AHE ρ_{AHE} curves and Nernst ΔS_{xy} curves, respectively, for sample Z5 at selected θ measured at 2.5 K (**c**) and 8 K (**d**). The variations of the AHE and Nernst signals versus θ are shown in the insets. The close similarities suggest that the two signals have the same origin.

Next, we consider rotating **H** within the *bc* plane. In this case, the out-of-plane (*ab*-plane) and in-plane (*ac*-plane) contributions combine to produce an AHE signal that displays mixed behaviour, as shown in Fig. 3g–i. The amplitude of the anomalous Hall signal $\rho_{AHE}(\theta)$ in the *bc* plane ($\varphi = -90°$), shown by the red line in Fig. 3i, is neither symmetric nor antisymmetric with respect to variations in θ. Interestingly, if we antisymmetrize ρ_{AHE} with respect to θ to define $\rho_A(\theta) \equiv (\rho_{AHE}(\theta) - \rho_{AHE}(-\theta))/2$ (dark cyan line in Fig. 3i), we obtain a profile similar to that obtained for the case of out-of-plane rotation (*ab* plane) shown in Fig. 3c. This suggests that the contribution from the *b* axis can be simply obtained as the projection of the magnetic field onto the *b* axis. In contrast, the in-plane (*ac*-plane) contribution cannot be obtained by the corresponding symmetrization process $\rho_S(\theta) \equiv (\rho_{AHE}(\theta) + \rho_{AHE}(-\theta))/2$ (olive line in Fig. 3i). In other words, a simple projection of **H** onto the *c* axis cannot reproduce the results. This suggests that there might be two kinds of Weyl pair, which respond differently to the applied magnetic field.

Finally, the *T* dependence of the AHE provides further evidence for the Weyl node origin (see Fig. 4). As seen in Fig. 4a, the negative LMR, suggestive of the chiral anomaly originating from the Weyl nodes, starts to become prominent below about 60 K. The AHE signal shows a similar onset—it is first resolved at 60 K, and then increases strongly as *T* decreases to 2.5 K (Fig. 4b). The close correlation between the negative LMR and the AHE further supports the Weyl node origin of the AHE.

We briefly discuss the results of the anomalous Nernst effect (ANE) shown in Fig. 4c,d. Since the AHE is observed for $ZrTe_5$, it is natural to expect that the system also shows an ANE. The Nernst effect is often more sensitive to transverse currents than is the Hall signal[31–33]. Figure 4c,d shows the angular dependence of the AHE and ANE for sample Z5. The close relation implies the same origin for the AHE and the ANE. For recent ANE work on Mn_3Sn, we refer the reader to ref. [34].

One potential scenario for Weyl nodes appearing in $ZrTe_5$ is that, since the energy gap Δ at the Γ point is small, Weyl nodes can be induced when the time-reversal symmetry is broken by a large Zeeman energy under an applied magnetic field with strength *B*, which splits the bands at the Γ point. When $\Delta = (g_v + g_c)\mu_B B/2$ is satisfied, the gap closes and the Weyl nodes appear. Here, g_v, g_c are the *g* factors for the valence and conduction bands, respectively. The other possibility is that, since $ZrTe_5$ is located near the boundary of a weak topological insulator and a strong topological insulator[25], if the inversion symmetry is broken in the system and there is a slight change in lattice parameter, the system automatically falls into a Weyl semimetallic phase, according to the general phase diagram proposed in earlier studies[1,2,35,36]. The fact that the anomaly of the resistivity occurs at $T_0 \lesssim 5$ K for our $ZrTe_5$ samples is suggestive of a subtle difference in doping or lattice constant in our samples compared with samples with $T_0 = 135$ K. Because the inversion-symmetry-broken Weyl states contain at least four Weyl nodes, or two kinds of Weyl pair, it would be interesting to investigate how they respond to an applied magnetic field. Our results indicate that exploring whether the inversion symmetry is broken in $ZrTe_5$ and how the Weyl nodes appear would be interesting directions to pursue in future research.

Methods

Methods, including statements of data availability and any associated accession codes and references, are available at https://doi.org/10.1038/s41567-018-0078-z.

Received: 14 August 2017; Accepted: 3 January 2018;
Published online: 19 March 2018

References

1. Murakami, S. & Kuga, S.-i Universal phase diagrams for the quantum spin Hall systems. *Phys. Rev. B* **78**, 165313 (2008).
2. Okugawa, R. & Murakami, S. Dispersion of Fermi arcs in Weyl semimetals and their evolutions to Dirac cones. *Phys. Rev. B* **89**, 235315 (2014).
3. Hosur, P. & Qi, X. Recent developments in transport phenomena in Weyl semimetals. *C. R. Phys.* **14**, 857–870 (2013).
4. Burkov, A. A. & Kim, Y. B. Z_2. *Phys. Rev. Lett.* **117**, 136602 (2016).
5. Wan, X., Turner, A. M., Vishwanath, A. & Savrasov, S. Y. Topological semimetal and Fermi-arc surface states in the electronic structure of pyrochlore iridates. *Phys. Rev. B* **83**, 205101 (2011).
6. Yang, K.-Y., Lu, Y.-M. & Ran, Y. Quantum Hall effects in a Weyl semimetal: possible application in pyrochlore iridates. *Phys. Rev. B* **84**, 075129 (2011).
7. Young, S. M. et al. Dirac semimetal in three dimensions. *Phys. Rev. Lett.* **108**, 140405 (2012).
8. Liang, T. et al. Ultrahigh mobility and giant magnetoresistance in the Dirac semimetal Cd_3As_2. *Nat. Mater.* **14**, 280–284 (2015).
9. Yang, L. X. et al. Weyl semimetal phase in the non-centrosymmetric compound TaAs. *Nat. Phys.* **11**, 728–732 (2015).
10. Lv, B. Q. et al. Experimental discovery of Weyl semimetal TaAs. *Phys. Rev. X* **5**, 031013 (2015).
11. Li, Q. et al. Chiral magnetic effect in $ZrTe_5$. *Nat. Phys.* **12**, 550–554 (2016).
12. Adler, S. L. Axial-vector vertex in spinor electrodynamics. *Phys. Rev.* **177**, 2426–2438 (1969).
13. Bell, J. S. & Jackiw, R. A PCAC puzzle: $\pi 0 \rightarrow \gamma\gamma$ in the σ-model. *Nuovo Cim. A* **60**, 47–61 (1969).
14. Nielsen, H. & Ninomiya, M. A no-go theorem for regularizing chiral fermions. *Phys. Lett. B* **105**, 219–223 (1981).
15. Xiong, J. et al. Evidence for the chiral anomaly in the Dirac semimetal Na_3Bi. *Science* **350**, 413–416 (2015).
16. Hirschberger, M. et al. The chiral anomaly and thermopower of Weyl fermions in the half-Heusler GdPtBi. *Nat. Mater.* **15**, 1161–1165 (2016).
17. Wang, Z. et al. Dirac semimetal and topological phase transitions in A_3Bi (A = Na, K, Rb). *Phys. Rev. B* **85**, 195320 (2012).
18. Wang, Z., Weng, H., Wu, Q., Dai, X. & Fang, Z. Three-dimensional Dirac semimetal and quantum transport in Cd_3As_2. *Phys. Rev. B* **88**, 125427 (2013).
19. Wu, R. et al. Evidence for topological edge states in a large energy gap near the step edges on the surface of $ZrTe_5$. *Phys. Rev. X* **6**, 021017 (2016).
20. Zhang, Y. et al. Electronic evidence of temperature-induced Lifshitz transition and topological nature in $ZrTe_5$. *Nat. Commun.* **8**, 15512 EP (2017).
21. Manzoni, G. et al. Ultrafast optical control of the electronic properties of $ZrTe_5$. *Phys. Rev. Lett.* **115**, 207402 (2015).
22. Shen, L. et al. Spectroscopic evidence for the gapless electronic structure in bulk $ZrTe_5$. *J. Electron Spectrosc. Relat. Phenom.* **219**, 45–52 (2016).
23. Xiong, H. et al. Three-dimensional nature of the band structure of $ZrTe_5$ measured by high-momentum-resolution photoemission spectroscopy. *Phys. Rev. B* **95**, 195119 (2017).
24. Fang, Z. et al. The anomalous Hall effect and magnetic monopoles in momentum space. *Science* **302**, 92–95 (2003).
25. Weng, H., Dai, X. & Fang, Z. Transition-metal pentatelluride $ZrTe_5$ and $HfTe_5$: a paradigm for large-gap quantum spin Hall insulators. *Phys. Rev. X* **4**, 011002 (2014).
26. Littleton, R. T. et al. Effect of Ti substitution on the thermoelectric properties of the pentatelluride materials $M_{1-x}Ti_xTe_5$ (M = Hf, Zr). *Appl. Phys. Lett.* **72**, 2056–2058 (1998).
27. Lowhorn, N. D., Tritt, T. M., Abbott, E. E. & Kolis, J. W. Effect of rare earth doping on the thermoelectric and electrical transport properties of the transition metal pentatelluride $HfTe_5$. In *ICT 2005. 24th Int. Conf. on Thermoelectrics, 2005* 41–45 (2005).
28. Fuller, W. et al. Pressure effects in $HfTe_5$ and $ZrTe_5$. *J. Phys. Colloques* **44**, 1709–1712 (1983).
29. Burkov, A. A. Giant planar Hall effect in topological metals. *Phys. Rev. B* **96**, 041110 (2017).
30. Nandy, S., Sharma, G., Taraphder, A. & Tewari, S. Chiral anomaly as the origin of the planar Hall effect in Weyl semimetals. *Phys. Rev. Lett.* **119**, 176804 (2017).
31. Behnia, K., Méasson, M.-A. & Kopelevich, Y. Oscillating Nernst–Ettingshausen effect in bismuth across the quantum limit. *Phys. Rev. Lett.* **98**, 166602 (2007).
32. Zhu, Z., Fauqué, B., Fuseya, Y. & Behnia, K. Angle-resolved Landau spectrum of electrons and holes in bismuth. *Phys. Rev. B* **84**, 115137 (2011).
33. Zhu, Z. et al. Quantum oscillations, thermoelectric coefficients, and the Fermi surface of semimetallic Wte_2. *Phys. Rev. Lett.* **114**, 176601 (2015).
34. Li, X. et al. Anomalous Nernst and Righi–Leduc effects in Mn_3Sn: Berry curvature and entropy flow. *Phys. Rev. Lett.* **119**, 056601 (2017).
35. Murakami, S. Phase transition between the quantum spin Hall and insulator phases in 3D: emergence of a topological gapless phase. *New J. Phys.* **9**, 356 (2007).
36. Murakami, S. Gap closing and universal phase diagrams in topological insulators. *Physica E* **43**, 748–754 (2011).

Acknowledgements

The research was supported by the US Army Research Office under contract ARO W911NF-16-1-0116. N.P.O. acknowledges the support of the Gordon and Betty Moore Foundation's EPiQS Initiative through grant GBMF4539. The crystal growth was carried out by Q.G., S.K. and R.J.C., with support from the US National Science Foundation (NSF MRSEC grant DMR 1420541). J.A.S., P.S.K. and Z.-X. S. were supported by the US Department of Energy, Office of Science, Basic Energy Sciences, Materials Sciences and Engineering Division under contract DE-AC02-76SF00515. T.L., J.A.S. and H.X. acknowledge support by the Gordon and Betty Moore Foundation's EPiQS Initiative through grant GBMF4546. Use of the Stanford Synchrotron Radiation Lightsource, SLAC National Accelerator Laboratory, is supported by the US Department of Energy, Office of Science, Office of Basic Energy Sciences under contract DE-AC02-76SF00515.

Author contributions

T.L. and N.P.O. conceived the idea behind the experiment. T.L. designed the experiment with double-axis rotator and carried out the transport measurements with some assistance from J.L., M.L. and W.W. The crystals were grown and characterized by Q.G., S.K. and R.J.C. The high-momentum-resolution laser-ARPES measurements were made and studied by H.X., J.A.S., P.S.K. and Z.-X.S. Synchrotron ARPES measurements at beamline 5-4 of SSRL were made by T.L. and M.H. Analyses of the measurements were carried out by T.L. and N.P.O. The manuscript was written by T.L. and N.P.O. All authors discussed the results and commented on the manuscript.

Competing interests

The authors declare no competing interests.

Additional information

Supplementary information is available for this paper at https://doi.org/10.1038/s41567-018-0078-z.

Reprints and permissions information is available at www.nature.com/reprints.

Correspondence and requests for materials should be addressed to T.L. or N.P.O.

Publisher's note: Springer Nature remains neutral with regard to jurisdictional claims in published maps and institutional affiliations.

Methods

Three-dimensional full 4π solid-angular-dependent transport measurements were made using a standard six-contact method with a home-made double-axis rotator installed on a commercial Physical Property Measurement System (PPMS; manufactured by Quantum Design, Inc.). In the main text, we take axis $\hat{x}||a$, $\hat{y}||c$ and $\hat{z}||b$. The high-momentum-resolution laser-ARPES measurements were carried out using a Scienta R4000 electron analyser and 6.0 eV ultraviolet light generated from a Ti:sapphire oscillator with photon energy quadrupling through two stages of second-harmonic generation. The energy, angular and momentum resolutions for this set-up are 10 meV, 0.3° and 0.004 $Å^{-1}$, respectively. Samples were cleaved in situ at a base pressure lower than 5×10^{-11} torr. ARPES measurements at beamline 5-4 at the Stanford Synchrotron Radiation Lightsource (SSRL) in the Stanford Linear Accelerator Center were made with 9 eV incident photon energy. Samples were cleaved in situ between 10 and 20 K at a chamber pressure lower than 5×10^{-11} torr.

Data availability. The data that support the plots within this paper and other findings of this study are available from the corresponding author upon reasonable request.